Delft University of Technology

Sedimentation and resistance tensor of a river floc from 3D X-ray microtomography

Gu, Chuan; Li, Heng; Spencer, Kate L.; Botto, Lorenzo

DOI
10.1016/j.ijmultiphaseflow.2025.105586

Licence
CC BY

Publication date
2026

Document Version
Final published version

Published in
International Journal of Multiphase Flow

Citation (APA)
Gu, C., Li, H., Spencer, K. L., & Botto, L. (2026). Sedimentation and resistance tensor of a river floc from 3D X-ray microtomography. *International Journal of Multiphase Flow*, *196*, Article 105586. https://doi.org/10.1016/j.ijmultiphaseflow.2025.105586

Important note
To cite this publication, please use the final published version (if applicable).
Please check the document version above.

Copyright
Other than for strictly personal use, it is not permitted to download, forward or distribute the text or part of it, without the consent of the author(s) and/or copyright holder(s), unless the work is under an open content license such as Creative Commons.

Takedown policy
Please contact us and provide details if you believe this document breaches copyrights.
We will remove access to the work immediately and investigate your claim.

This work is downloaded from Delft University of Technology.
For technical reasons the number of authors shown on this cover page is limited to a maximum of 10.

International Journal of Multiphase Flow 196 (2026) 105586

Contents lists available at ScienceDirect

International Journal of Multiphase Flow

journal homepage: www.elsevier.com/locate/ijmulflow

Research Paper

Sedimentation and resistance tensor of a river floc from 3D X-ray microtomography

Chuan Gu [a], Heng Li [b], Kate L. Spencer [c], Lorenzo Botto [b,*]

[a] School of Engineering and Materials Science, Queen Mary University of London, London, E1 4NS, United Kingdom
[b] Department of Process & Energy, Faculty of Mechanical Engineering, Delft University of Technology, Delft, 2628 CB, The Netherlands
[c] School of Geography, Queen Mary University of London, London, E1 4NS, United Kingdom

ARTICLE INFO

Keywords:
Particulate flow
Anisotropic particle
Sedimentation
Particle simulation

ABSTRACT

Natural sediment flocs are highly porous particulate aggregates composed of biogenic and minerogenic materials. They can be an important component of suspended sediment load in rivers, estuaries and the marine environment and modelling floc dynamics and behaviour is very important for many aquatic industries, maintenance of waterways and conservation and management of aquatic water bodies. X-ray computed microtomography has recently been applied to quantify the complex three-dimensional (3D) geometry of natural sediment flocs. Here, X-ray images of 3 selected natural millimetre-sized flocs sampled from the Thames River have been digitalised and converted into geometries used in Stokesian Dynamics calculations of the hydrodynamic properties of the flocs, where each floc is represented as a rigid ensemble of spherical beads moving in the creeping flow regime. Our approach is a substantial step from previous attempts in which synthetic fractal structures were simulated. In addition to describe the complex dynamics of floc settling, we compute: (i) the hydrodynamic radius of the flocs; (ii) the floc mobility and resistance tensors; and (iii) the relation between sedimentation velocity and fractal dimension. The simulations show that the coupling of gravitational forces with lateral velocities, which we analysed by examining the cross-components of the mobility matrix, produces a helical motion of the flocs as they settle. We argue that this lateral motion may lead to an enhancement of floc–floc aggregation by differential sedimentation due to an increase in the effective collisional area. Furthermore, the simulations demonstrate significant differences in the dynamics of settling between the three flocs despite a similar gross shape. Our work exemplifies how high-resolution X-ray techniques can be coupled with accurate particle-resolved simulations to understand the settling dynamics of real (as opposed to synthetic) flocs collected from estuarine, coastal or waste-water environments.

1. Introduction

Natural water bodies such as estuaries and coasts are usually characterised by high concentrations of fine-grained and cohesive sediments which are transported in suspension and can be highly variable in space and time. This suspended particulate matter (SPM) is critical for the transport of sediment, nutrients, carbon and pollutants from catchment to coast, and in excess can cause rapid sedimentation causing problems for navigation, deterioration to water quality and smothering of benthic habitats (Manning et al., 2017; Mehta, 2013; Zhu et al., 2022). Therefore, accurate modelling and prediction of the dynamics and in particular settling behaviour of fine sediments is crucial to the understanding and management of all natural fresh and marine water bodies and associated aquatic industries (Johnson et al., 1996; Kumar et al., 2010; Spearman and Manning, 2008; Dorrell and Hogg, 2010). Where fine sediment sources dominate, flocs are an important component of this suspended particulate matter. Fine sediments (clays and silts) are cohesive and in suspension aggregate to form loosely bound, highly irregular, fragile sediment flocs which comprise inorganic mineral particles, organic matter, microbial organisms and fluid-filled pore space (Liss et al., 1996; Droppo, 2001; Rahmani et al., 2022). Modelling approaches to predict the large-scale hydrodynamics of sediment in estuarine and coastal waters are well established including e.g., TELEMAC and DELFT3D (Lesser et al., 2004; Villaret et al., 2013). However, predicting the fate and behaviour of fine-grained and cohesive sediment is far more challenging. This is largely due to the failure to adequately represent floc dynamics in the model and predictions of cohesive sediment behaviour is often poor (Droppo et al., 1998; Li et al., 2025).

* Corresponding author.
E-mail address: l.botto@tudelft.nl (L. Botto).

https://doi.org/10.1016/j.ijmultiphaseflow.2025.105586
Received 17 September 2025; Received in revised form 24 November 2025; Accepted 21 December 2025
Available online 22 December 2025
0301-9322/© 2025 The Authors. Published by Elsevier Ltd. This is an open access article under the CC BY license (http://creativecommons.org/licenses/by/4.0/).

Floc settling velocity is dependent upon floc diameter, shape, density and porosity and these are critical input parameters required to mathematically predict their behaviour (Baugh and Manning, 2007). Consequently, investigations of floc dynamic behaviour frequently focus on estimating the floc settling velocity (Gibbs, 1985; Dyer and Manning, 1999; Derksen, 2014) and this is a key parameter in large-scale transport models used to predict fine or cohesive sediment transport particularly within the estuarine environment and when estimating the distribution and fate of fine sediment and contaminant plumes associated with e.g., dredging activities. Floc size and shape are typically derived from two-dimensional (2D) observations of SPM aggregates using image analysis or laser diffraction (Agrawal and Pottsmith, 1994; Schwarz et al., 2017; Chapalain et al., 2019), whilst density and porosity are estimated and typically assume that flocs are spherical. However, the shape of natural sediment flocs is in fact highly irregular and settling velocity can be derived by establishing a relationship between floc density and size (Tambo and Watanabe, 1979). This can be achieved by assuming the flocs are self-similar, where a computationally simple fractal-based model assumes that floc structures are scale invariant, and is widely used to predict floc behaviour (e.g., settling velocity, rate of floc aggregation and disaggregation) (Kranenburg, 1994; Winterwerp and Van Kesteren, 2004; Smoczyński et al., 2016).

The estimation of settling velocity is most commonly based on the amended form of the Stokes' law which incorporates the effects of the floc shape, fractal dimension and finite inertia (Winterwerp, 1998). The variability of the floc fractal dimension as a function of floc size has been investigated by several authors including Khelifa and Hill (2006), Maggi et al. (2007), Vahedi and Gorczyca (2012). Some works have modelled floc aggregates as porous and permeable spheres (Veerapaneni and Wiesner, 1996; Kim and Stolzenbach, 2002; Lattuada et al., 2004), while some other investigations have modelled the aggregates as a collection of spherical primary spheres (Filippov et al., 2000; Binder et al., 2006; Harshe et al., 2010). By assuming that the floc is fractal, the excess weight of the floc is allowed to scale with the size of the floc as a power law of the floc fractal dimension. This is a simplification as floc shape can alter settling velocity directly, by altering the floc hydrodynamic mobility (Happel and Brenner, 2012). Flocs with asymmetric shapes can induce a coupling between the external force due to gravity and the angular velocity of the floc (Tozzi et al., 2011). The rotational motion of the floc is an important part of the floc settling behaviour that has often been overlooked in previous studies.

Despite the complexity of floc sedimentation, some general results on the settling (or sedimentation) velocity follow from basic fluid mechanics considerations. The importance of fluid inertia during settling is indicated by the particle Reynolds number $Re_p = u_s R_{en}/\nu$, where u_s is the settling velocity, ν is the kinematic viscosity of the surrounding liquid and R_{en} is the characteristic size of the particle (Koch and Hill, 2001; Zhang et al., 2006; Aidun et al., 1998), which in the case of flocs can be taken as the radius of the smallest sphere enclosing the floc. When $Re_p \ll 1$ the fluid flow in the vicinity of the floc is in the Stokes regime where the inertia of the fluid is negligible (see e.g. Ref. Maxey and Riley 1983). In this regime, the velocity of the floc must be a linear function of the external gravitational (gravity plus buoyancy) force, regardless of the shape of the floc (Happel and Brenner, 2012). In general, such a relationship is tensorial, implying that there is a coupling between the force in the gravitational direction and the velocities in the lateral direction, as well as the rotational velocity.

A sphere of course settles with a velocity that is parallel to the direction of gravity. However, this is not the case for particles of non spherical shape. Flocs will, in general, drift laterally as they settle. This can be shown by a simple derivation. If we call $\mathbf{F}^B$ the force vector due to buoyancy (Archimede's force), $\mathbf{F}^M$ the force vector due to weight, and $\mathbf{F}$ the hydrodynamic force due to the fluid, at steady state a force balance requires

$$\mathbf{F} + \mathbf{F}^B + \mathbf{F}^M = \mathbf{0} \tag{1}$$

To find the settling velocity, we need to relate the hydrodynamic force to velocity. In Stokes flow we can write, for any floc shape, a relation of the form

$$\mathbf{F} = -\mu \mathbf{R} \cdot \mathbf{U} \tag{2}$$

where $\mathbf{U}$ is the settling velocity vector, μ is the fluid dynamic viscosity, and $\mathbf{R}$ is the so-called resistance tensor (i.e. a matrix, in a given coordinate system). For a floc of homogeneous density ρ_s immersed in a fluid of density ρ_f, one can write $\mathbf{F}^M = \rho_s V \mathbf{g}$ and $\mathbf{F}^B = -\rho_f V \mathbf{g}$, where V is the volume occupied by the solid. Thus the settling velocity is:

$$\mathbf{U} = \frac{(\rho_s - \rho_f)V}{\mu} \mathbf{R}^{-1} \cdot \mathbf{g} \tag{3}$$

where $\mathbf{R}^{-1}$, the inverse of $\mathbf{R}$, is also called the mobility matrix. Because $\mathbf{R}^{-1}$ is a matrix, $\mathbf{U}$ will in general not be parallel to $\mathbf{g}$. If gravity is directed along the z axis, say, there will be a component of the settling velocity in the x and y directions. The aim of this paper is to study the resistance or mobility matrices using realistic floc geometries. To our knowledge this has not been previously considered due to the challenges of sampling and quantifying the 3D characteristics of fragile natural sediment flocs. While a characterisation of $\mathbf{R}$ and $\mathbf{R}^{-1}$ requires a certain level of mathematical analysis, the advantages are considerable. It is indeed impossible to fully characterise the settling velocity of an anisotropic body without characterising $\mathbf{R}$. Furthermore, $\mathbf{R}$ is an intrinsic property that depends only on the size and shape of the floc, thus information on $\mathbf{R}$ can be obtained from geometrical characteristics only.

With our work we also intend to challenge an assumption often made in practical modelling of floc sedimentation. The assumption is that the fractal dimension of the floc affects the effective weight of the floc, but not the hydrodynamic resistance (Spencer et al., 2021; Smoczyński et al., 2016; Xu and Dong, 2017; Chapalain et al., 2019).

The settling velocity is often calculated as

$$u_s = \frac{(\rho_s - \rho_w)gV}{\theta \mu \ell}, \tag{4}$$

where $(\rho_s - \rho_w)gV$ is the excess weight of the floc, ℓ is the characteristic size of the floc, and θ is a dimensionless shape factor for the drag force (for a sphere, $\theta = 6\pi$ and ℓ is the radius). For a fractal-like floc, the floc volume V scales with its characteristic size ℓ according to

$$\frac{V}{V_0} \propto \left(\frac{\ell}{\ell_0}\right)^{D_f} \tag{5}$$

where V_0 and ℓ_0 are the volume and characteristic size of the primary particle. Assuming the primary particle of the floc is spherical with radius ℓ_0 we have $V_0 = \frac{4}{3}\pi \ell_0^3$, and we can express the settling velocity again as

$$u_s = \frac{4\pi k(\rho_s - \rho_w)g}{3\theta\mu} \ell^{D_f - 1} \ell_0^{3 - D_f}, \tag{6}$$

where k is another dimensionless shape factor for the volume scaling in Eq. (5). For a sphere, $\theta = 6\pi$, $k = 1$, $D_f = 3$, and Eq. (6) reduces to the Stokes velocity of a sphere. This Eq. (6) is of the same form with the expression of floc settling velocity presented in Winterwerp (1998) where differential density instead of volume is assumed to follow the fractal scaling (Kranenburg, 1994). The ratio between the settling velocity of the floc and the Stokes velocity of the primary sphere is $\frac{6\pi k}{\theta}\left(\frac{l}{l_0}\right)^{D_f - 1}$. As we can see explicitly from Eq. (5), the excess weight depends purely on geometry. In the current paper we are able to calculate D_f for flocs that have a realistic geometry (as opposed to a synthetic fractal geometry), and compute the hydrodynamic parameter θ for the same geometry. In the paper, we prefer to discuss the hydrodynamic radius of the floc, rather than θ, but the relation between the two is obvious once the characteristic size of the floc is set.

In this work, we employ the Stokesian dynamics method (Brady and Bossis, 1988) to investigate numerically the settling behaviours of the

Table 1
The list of the flocs with realistic geometry used in the current work. The length, width and height of the bounding box of the flocs are L, W, H respectively, N_v is the number of voxels of the floc 3D image and R_{en} is the radius of the smallest enclosing sphere of the floc. The length is expressed in unit of μm.

Code name	L	W	H	N_v	R_{en}
S4	754.5	1770.5	2122.6	190 973	1113.1
S5	2494.8	2756.4	4537.0	494 540	2489.9
S6	1629.4	996.6	2151.5	61 691	1186.5

three flocs having realistic geometry. The Stokesian dynamics method assumes a negligible effect of fluid inertia. This is a good assumption for river flocs, which have a low effective density and therefore settle slowly: for example, for a floc with diameter 100 μm settling in water at a typical velocity 1 mm/s (Ali et al., 2024), the Reynolds number of the floc is around 0.1. The structure of the flocs is modelled as an aggregate of spherical beads whose radius can be adjusted to modulate the spatial resolution of the aggregate structure. The realistic floc geometries were extracted from the 3D greyscale images of flocs generated using X-ray computed microtomography (CT) (Wheatland et al., 2017, 2020). The sediments were collected from the Thames Estuary, UK and are fine-grained silts and clays. While much work has been done on modelling a floc as a synthetic fractal, regular assembly of spheres, or bead aggregates generated by stochastic algorithms, the current paper analyse flocs that, from a geometric point of view, have truly realistic three-dimensional features.

2. Extracting floc shape from X-ray CT images

The experimental methodology to extract the 3D greyscale images of flocs generated using X-ray computed microtomography is described in a series of previous publications (Wheatland et al., 2020; Lawrence et al., 2022; Spencer et al., 2022). Briefly, the protocol involves settling flocs directly into plankton chambers and immobilising flocs in agarose gel. The gel is used to minimise deformation of the very fragile flocs during sample handling as this was placed in sample holders and mounted on the stage of a micro-computed tomography (micro-CT) machine at the School of Engineering and Materials Science at Queen Mary University of London. The micro-CT machine maps the attenuation of X-rays that cross the sample, giving cross-sectional images of the density of each floc from μm to mm-scale. The micro-CT software assemble multiple cross-sectional images to reconstruct a fully three-dimensional image of the floc. Notice that the flocs are very fragile and this has made the technical hurdles of obtaining the X-ray images uniquely challenging, as described in our previous publications (Wheatland et al., 2020; Lawrence et al., 2022; Spencer et al., 2022). This is why only a few flocs could be analysed.

In this work, 3 flocs were analysed in detail. The characteristics of each floc are summarised in Table 1, where the flocs are labelled as flocs S4, S5 and S6. Visualisation of the 3D floc geometry through X-ray computed microtomography generates a binary voxel image of the floc, with a pixel resolution of 2.78 μm. The voxel image of each floc is shown in Fig. 1.

The voxel images were used for sedimentation simulations. In the literature, two classes of modelling approaches have been used to analyse the hydrodynamic properties of flocs of aggregated particles. In the first approach the floc is modelled as a porous sphere whose porosity and permeability are functions of the fractal dimension of the floc (Johnson et al., 1996; Kim and Yuan, 2005; Veerapaneni and Wiesner, 1996; Vanni, 2000). In the creeping flow regime, Brinkman's equation for the flow inside the sphere is coupled to the Stokes equation outside of the sphere This approach models the internal structure of the particle as a continuum and requires the knowledge of the distribution of the permeability coefficient. The second approach models the structure of the particle as an assemblage of spherical beads. This modelling approach was first proposed by Kirkwood and Riseman (1948) to study the hydrodynamic properties of macromolecules in solution. The methodology was later extensively studied by Bloomfield et al. (1967a,b), McCammon and Deutch (1976), Swanson et al. (1978), using the modified-Oseen tensors to more accurately describe hydrodynamic interactions between primary beads (Rotne and Prager, 1969; Yamakawa, 1970). A comparison of several methods to assemble the beads into an aggregate to perform hydrodynamic calculations can be found in Carrasco and de la Torre (1999). We use this second approach, using the Stokesian Dynamics method (Brady and Bossis, 1988) to account for the hydrodynamic interactions between the spherical beads composing the aggregate. In our method, all the beads are assumed to have the same radius and mass density.

A stochastic procedure is employed in the current work to generate the aggregate from the 3D voxel image of the floc. First, the radius a of the sphere is prescribed according to the required spatial resolution. Secondly, a voxel of the floc 3D image is randomly selected following an uniform probability distribution. A random location inside the selected voxel is then selected, also following a uniform distribution, and the first sphere is placed at this coordinate. The voxel selection and placement of spheres is repeated in a loop. In the algorithm, a sphere placement step is accepted as long as the sphere does not overlap with any existing spheres. Otherwise, the current sphere placement is rejected and a new location proposed until a valid location is found. After a sphere is placed inside a voxel, the voxel selection and sphere placement within a voxel are repeated until no more spheres can be placed within any voxel of the floc. A schematic of the resulting sphere aggregate generated from the digitised image is shown in Fig. 2. The use of a uniform probability distribution ensures that all locations within the region occupied by the voxels have the same probability of being associated with the centre of a spherical bead.

The geometry of the aggregates of spherical beads resulting from the algorithm are a close representation of the images of the initial floc, as can be seen by comparing Figs. 1 and 3. Changing the bead radius a enables to represent the digitised images at different coarseness levels. Thus, by varying a we can analyse how faithfully we need to represent the digitised floc to obtain hydrodynamic properties of converged values. Of course, the digitised images are also a discrete model of a real floc, so examining the limit $a \to 0$ will give only an approximation of the true hydrodynamic properties of the sampled natural floc. However, if the values of the hydrodynamic properties are relatively insensitive to the value of a, then we can conclude that the resolution of the experimental imaging method was sufficient to extract the hydrodynamic properties of the floc.

3. Simulation method and structure of the mobility and resistance matrices

The method of Stokesian dynamics was originally developed to simulate the hydrodynamics of a suspension of freely-moving spheres in the Stokes regime (Brady and Bossis, 1988).

This method relies on the fact that in the Stokes flow regime the vector relation between the hydrodynamic forces and torques on all the particles and the corresponding particle translational and angular velocity vectors must be linear, and therefore can be recast in matrix form (a generalisation of Stokes' law, where the force on a single particle is proportional to the relative particle–fluid velocity). For a suspension of N spheres, we can write (Brady and Bossis, 1988)

$$\begin{bmatrix} \mathbf{U} - \mathbf{U}^{\infty} \\ -\mathbf{E}^{\infty} \end{bmatrix} = -\mathcal{M} \cdot \begin{bmatrix} \mathbf{F}^{H} \\ \mathbf{S} \end{bmatrix}, \tag{7}$$

where $\mathbf{U}-\mathbf{U}_{\infty}$ is a $6N$-dimensional vector representing the translational and angular velocity difference between the spheres and the undisturbed fluid, $\mathbf{E}_{\infty}$ is the N-dimensional vector of the imposed rate of strain at the location of each sphere, $\mathbf{F}^{H}$ is the $6N$-dimensional vector

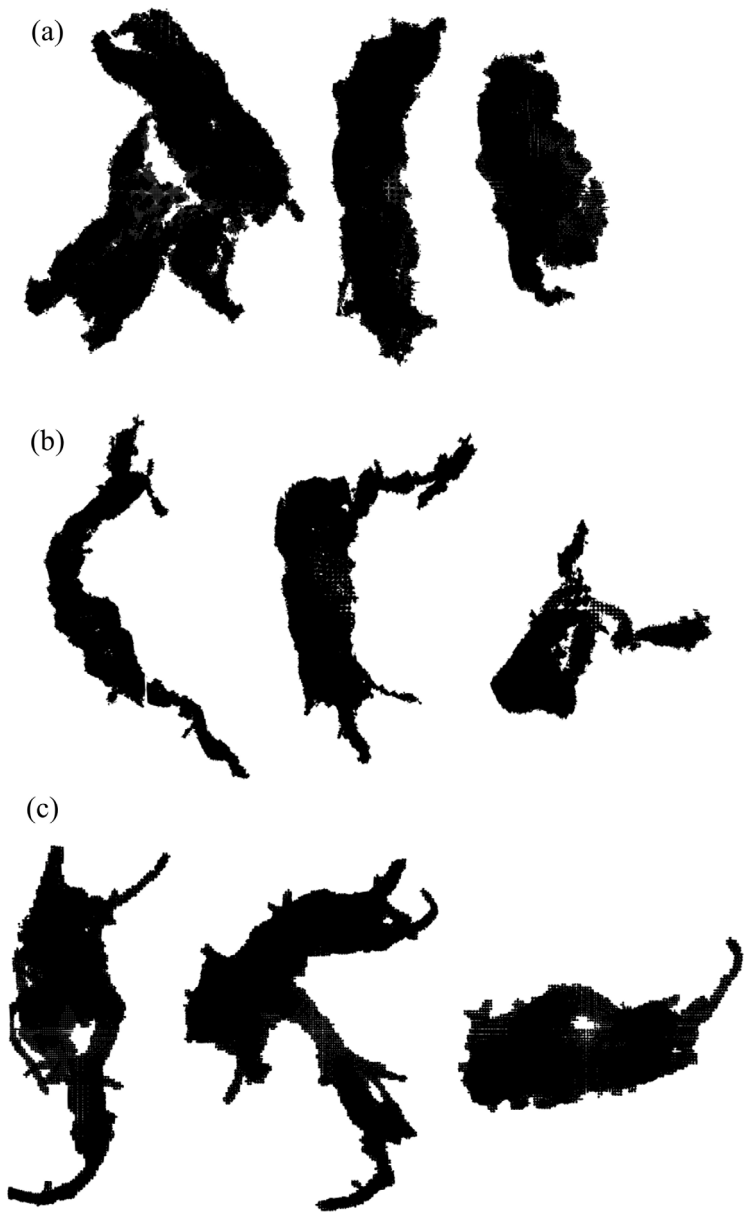

Fig. 1. The binary voxel image of the floc (*a*) S4, (*b*) S5 and (*c*) S6 from different angles. The scale of each image is adjusted to maximise the floc inside each picture.

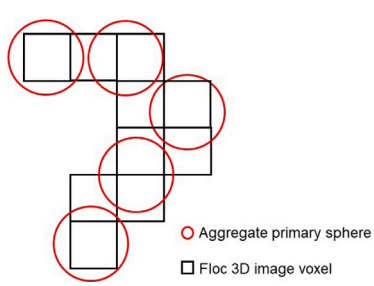

Fig. 2. The spheres (red sphere) are placed inside the voxels of the floc (black cube). The resulting aggregate of spheres is the geometric model which we use to study the hydrodynamic properties of the floc. (For interpretation of the references to colour in this figure legend, the reader is referred to the web version of this article.)

of the hydrodynamic forces and torques, and $\mathbf{S}$ is the N-dimensional vector containing the components of the "stresslet" corresponding to each sphere. Importantly, in Eq. (7) the *grand mobility matrix* $\mathcal{M}$ is only a function of the configuration of the spheres and its matrix properties – including eigenvalues and eigenvectors – fully determine the coupling between the external body forces applied to the floc and the sedimentation velocity of the floc. The grand mobility matrix $\mathcal{M}$ can be partitioned into four submatrices

$$\mathcal{M} = \begin{bmatrix} \mathbf{M}_{UF} & \mathbf{M}_{US} \\ \mathbf{M}_{EF} & \mathbf{M}_{ES} \end{bmatrix}. \tag{8}$$

where the subscript in each submatrix indicates the relevant coupling. For instance, $\mathbf{M}_{UF}$ couples the generalised velocity vector $\mathbf{U}$ to the generalised force vector $\mathbf{F}^H$.

For sedimentation in a quiescent fluid, we have $\mathbf{E}_\infty = \mathbf{0}$ (no fluid velocity gradient in the absence of the particles) and $\mathbf{U}^\infty = 0$ (zero uniform velocity in the absence of the particles), thus the vector of

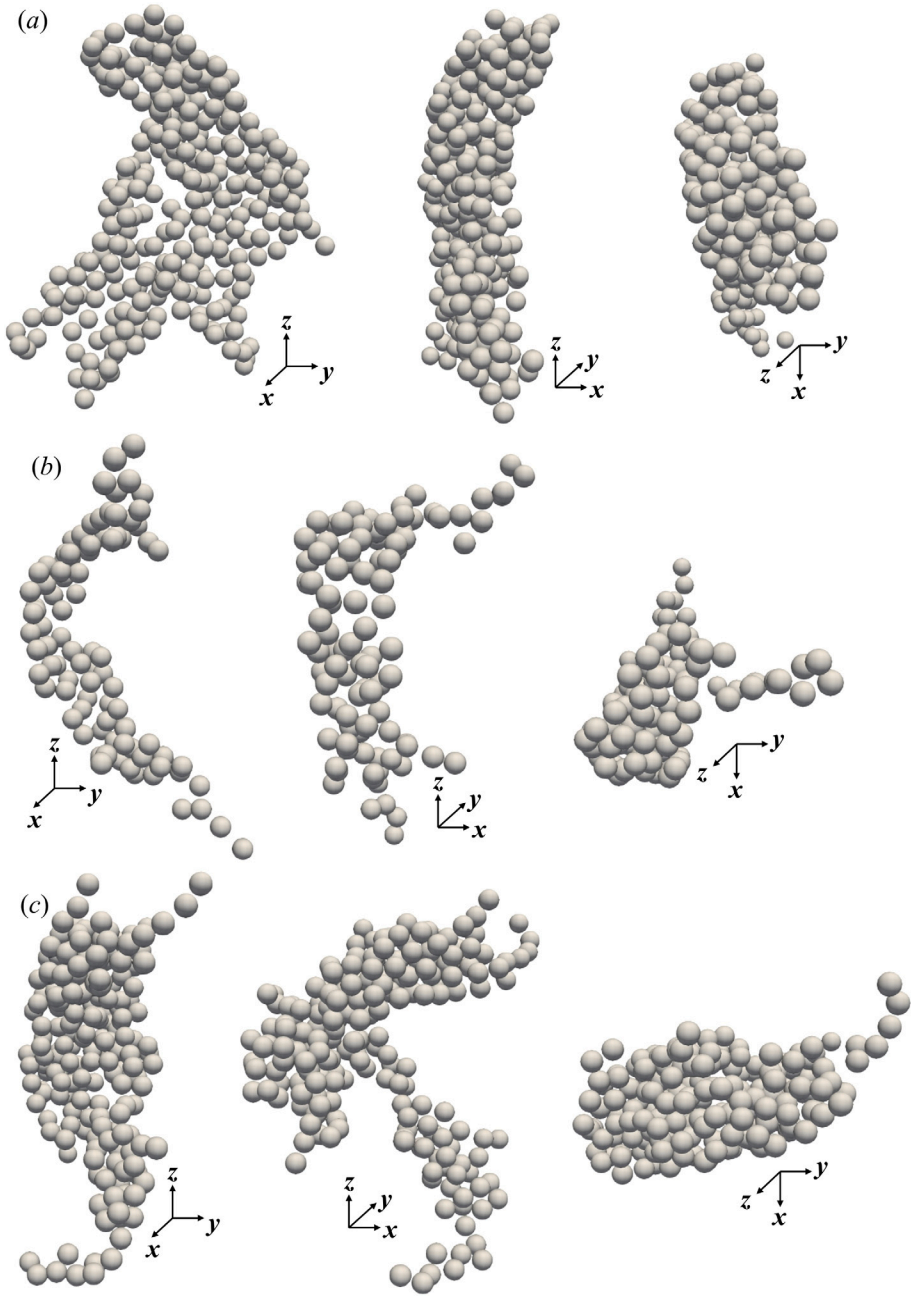

Fig. 3. Three aggregates of spherical beads generated by the volume sampling method to represent the floc (*a*) S4, (*b*) S5 and (*c*) S6 respectively, corresponding to the voxel images shown in Fig. 1. The spherical bead radius $a = R_{en}/20$.

sphere velocities obeys

$$\mathbf{U} = \mathbf{M}_{UF} \cdot \mathbf{F}, \tag{9}$$

where

$$\mathbf{U} = \begin{bmatrix} \mathbf{u} \\ \boldsymbol{\omega} \end{bmatrix}. \tag{10}$$

and

$$\mathbf{F} = \begin{bmatrix} \mathbf{f} \\ \mathbf{t} \end{bmatrix}. \tag{11}$$

Here $\mathbf{f}$ and $\mathbf{t}$ are the vectors of forces and torques on the spheres due to weight and buoyancy. The expression for $\mathbf{F}$ takes into account that for inertialess particles the hydrodynamic force and torque on each sphere balance the corresponding external force and torque due to gravity and buoyancy, $\mathbf{F}^H = -\mathbf{F}$. The vector $\mathbf{U}$ includes the translational velocity $\mathbf{u}$ and rotational velocity $\boldsymbol{\omega}$ of each sphere composing the floc.

If Eq. (9) was used without additional constraints, the relative position of the spheres, and thus the mobility tensor, would change in time. To model a rigid floc, an additional constraint must therefore be enforced on each sphere so that the entire group of spheres translates and rotates according to a rigid body motion (Swan et al., 2011; Yu and Niu, 2024; Harshe and Lattuada, 2012). This constraint is enforced by transforming the *resistance tensor of the free suspension*, $\mathbf{R}_{FU} = \mathbf{M}_{UF}^{-1}$, into the *resistance tensor of the rigid aggregate*, $\mathbf{R}_f$ by using the relation (Swan et al., 2011)

$$\mathbf{R}_f = \mathbf{K} \cdot \mathbf{R}_{FU} \cdot \mathbf{K}^T. \tag{12}$$

Here $\mathbf{K}$ is a tensor transforming the velocities of the free spheres into velocities following a rigid body motion. The matrix $\mathbf{K}$ is composed

of a number N of 6×6 submatrices $\begin{pmatrix}\mathbf{K}_1 & \mathbf{K}_2 & \mathbf{K}_3 & \cdots & \mathbf{K}_N.\end{pmatrix}$, one submatrix for each sphere. The submatrix for sphere α is only a function of the coordinates $(x_\alpha, y_\alpha, z_\alpha)$ of sphere α and of the centre $\mathbf{x}_0 = (x_0, y_0, z_0)$ around which the rigid body motion occurs. The structure of the $\mathbf{K}_\alpha$ matrix, $\alpha = 1...N$, is

$$\mathbf{K}_\alpha = \begin{bmatrix} 1 & 0 & 0 & 0 & 0 & 0 \\ 0 & 1 & 0 & 0 & 0 & 0 \\ 0 & 0 & 1 & 0 & 0 & 0 \\ 0 & -(z_\alpha - z_0) & y_\alpha - y_0 & 1 & 0 & 0 \\ z_\alpha - z_0 & 0 & -(x_\alpha - x_0) & 0 & 1 & 0 \\ -(y_\alpha - y_0) & x_\alpha - x_0 & 0 & 0 & 0 & 1 \end{bmatrix}. \tag{13}$$

Evidently we can describe a rigid body motion with respect to any point inside a rigid object. Therefore the point $\mathbf{x}_0$ is arbitrary. However, a specific choice for $\mathbf{x}_0$ makes the formulation simpler to analyse and the algorithm easier to implement. For any configuration of the rigid aggregate, a point exists for which the total torque on the rigid object produced by weight and buoyancy is zero. This point is called the centre of action (CA) of the body (Bernal and De La Torre, 1980), and is here denoted as $\mathbf{x}_{CA}$. For a rigid distribution of spheres of mass m_α, the centre of action can be calculated from

$$\mathbf{x}_{CA} = \frac{\sum_{\alpha=1}^{n} \left(m_\alpha - m_f^\alpha\right) \mathbf{x}_\alpha}{\sum_{\alpha=1}^{n} \left(m_\alpha - m_f^\alpha\right)}, \tag{14}$$

where m_f^α is the mass of the liquid displaced by sphere α and $\mathbf{x}_\alpha = (x_\alpha, y_\alpha, z_\alpha)$. In our case, we assume that all the spheres have the same radius and density, so the centre of action coincides with the geometric centre of the aggregate (centroid):

$$\mathbf{x}_{CA} = \frac{1}{N} \sum \mathbf{x}_\alpha. \tag{15}$$

The more general expression (14) should be used in the interesting case in which one accounts for inhomogeneities in the mass distribution.

We set $\mathbf{x}_0 = \mathbf{x}_{CA}$. By doing so, the calculation of the translational and rotational velocities of the floc requires only the force on each particle composing the floc, but not the moment of this force, which is a considerable simplification, both algorithmically and in terms of theoretical analysis of the settling velocity.

The algorithm to update the configuration of the floc works as follows. We first calculate $\mathbf{R}_{FU}$ (how to assemble the matrix is explained in Durlofsky et al. 1987 but Stokesian Dynamics solvers are also publicly available, see e.g. Swan et al. 2011). Then we calculate $\mathbf{K}$ by assembling matrices $\mathbf{K}_\alpha$ with $\mathbf{x}_0 = \mathbf{x}_{CA}$. From $\mathbf{R}_{FU}$ and $\mathbf{K}$ we compute $\mathbf{R}_f$ by using Eq. (12). Finally, from $\mathbf{R}_f$ we compute the mobility matrix of the rigid aggregate by numerical matrix inversion: $\mathbf{M}_f = \mathbf{R}_f^{-1}$.

From the mobility matrix the 6-dimensional velocity vector $\mathbf{U}_f$ of the rigid floc, containing the 3 components of the translational velocity and the 3 components of the rotational velocity of the floc, can be easily calculated from

$$\mathbf{U}_f = \mathbf{M}_f \cdot \mathbf{F}_t. \tag{16}$$

In this expression the 6-dimensional vector $\mathbf{F}_t$ is given by

$$\mathbf{F}_t = \begin{pmatrix} \mathbf{f}_t \\ \mathbf{0} \end{pmatrix} = \mathbf{K} \cdot \left(\mathbf{F}_g + \mathbf{F}_b\right). \tag{17}$$

where $\mathbf{F}_g$ and $\mathbf{F}_b$ are, respectively, the $6N-$dimensional vectors of the weight and buoyancy forces on each sphere. Once $\mathbf{U}_f$ is known, the velocity of each sphere composing the floc is calculated as $\mathbf{U} = \mathbf{K}^T \mathbf{U}_f$. In our implementation, the coordinates $\mathbf{x}_\alpha$ are updated by integrating $\mathbf{U}$ in time via a four-step Adams–Bashforth method. Code validation was obtained by comparing against analytical solutions for a smooth sphere and for an asymptotically slender chain of spheres, see Fig. 6.

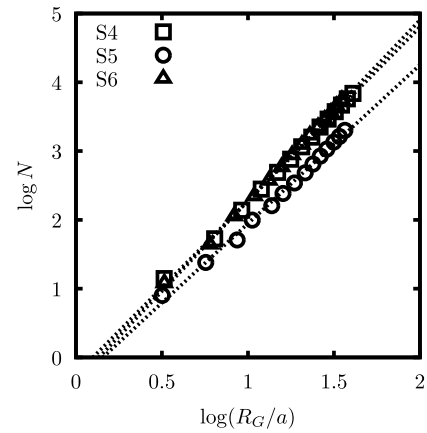

Fig. 4. The dependence of the number of spheres N composing the aggregates representing the floc S4, S5 and S6 on the normalised gyration radius R_G/a of the aggregates. The dashed lines are the best linear fit between $\log N$ and $\log(R_G/a)$ for each floc. The slope of each fit is an approximation of the fractal dimension D_f of the floc, being 2.53 for S4, 2.31 for S5 and 2.63 for S6.

4. Results

4.1. Fractal dimension and porosity

Before analysing the hydrodynamic simulations, we discuss the fractal dimension of our flocs, noting that a fractal dimension can be calculated whether the floc has a self-similar structure or not (Kim and Stolzenbach, 2002). For a rigid aggregate of identical spheres of radius a, the fractal dimension D_f is the power-law exponent between the number of spheres N and the radius of gyration R_G (Gmachowski, 1996):

$$N = k_f \left(\frac{R_G}{a}\right)^{D_f}, \tag{18}$$

Here k_f is a numerical prefactor (Sorensen and Roberts, 1997), and

$$R_G = \left[\frac{1}{N} \sum_i^N |\mathbf{x}_i - \mathbf{x}_m|^2\right]^{\frac{1}{2}} \tag{19}$$

where $\mathbf{x}_m$ is the arithmetic mean of the position vectors of the spheres constituting the aggregate. In Fig. 4, the number N of the spheres within an aggregate is plotted against the normalised aggregate size R_G/a on log–log scale for floc S4, S5 and S6. In this test, R_G is fixed while we change a. The fractal dimension of the floc D_f is measured from a linear fit between $\log N$ and $\log(R_G/a)$. The fractal dimensions of the floc S4 and S6 are comparable, being 2.53 and 2.63 respectively while for floc S5 it is 2.31. The lower fractal dimension of floc S5 correlates with it having a more ramified shape than $S4$ and $S6$.

Another important quantity used in the characterisation of aggregates is the floc porosity. The porosity of the fractal aggregates typically increases with floc size and is generally derived from density which is estimated from settling velocity assuming spherical shape (Droppo et al., 2000). In the current study, the porosity ϵ is calculated by normalising the total volume of the assembling spheres by the volume of the enclosing sphere, of radius R_{en} enclosing the aggregate. The result is

$$\epsilon = 1 - N\left(\frac{a}{R_{en}}\right)^3. \tag{20}$$

We characterise the radius of the enclosing sphere because this quantity is commonly used to estimate the drag force on the floc based on the drag formula for spheres (Guazzelli and Morris, 2011). We can

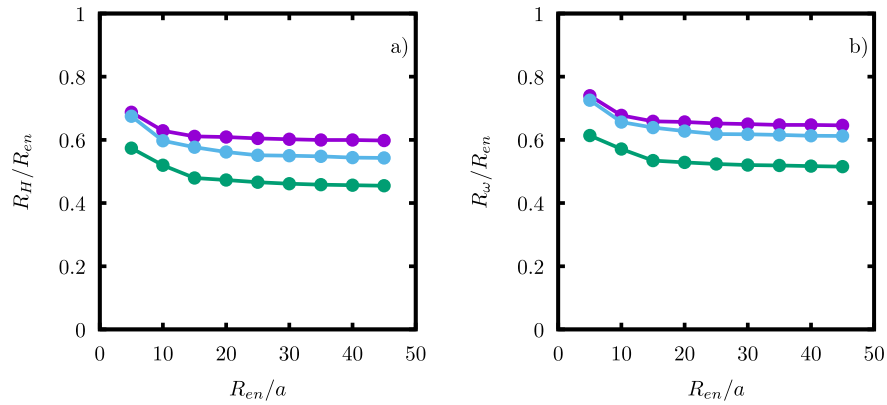

Fig. 5. The normalised (a) translational hydrodynamic radius R_H/R_{en} and (b) rotational hydrodynamic radius R_ω/R_{en} of floc S4 (purple), S5 (green) and S6 (light blue) are shown as a function of R_{en}/a. The value of R_{en}/a is varied by changing the primary sphere radius a while R_{en} is an intrinsic property of each floc and remains constant. (For interpretation of the references to colour in this figure legend, the reader is referred to the web version of this article.)

introduce the ratio $m = \frac{R_G}{R_{en}}$ of the radius of gyration of the floc to the radius of the enclosing sphere, and knowing Eq. (18) we have

$$\epsilon = 1 - k_f \left(\frac{R_{en}}{a}\right)^{D_f-3} m^{D_f} \tag{21}$$

This equation shows that if m is approximately constant and $D_f < 3$, ϵ increases with the floc diameter R_{en} for constant a. In other words, the porosity of the floc increases as the floc size increases.

4.2. Hydrodynamic radius

The mobility matrix $\mathbf{M}_f$ in Eq. (16) can be divided to four 3×3 sub-matrices, with $\mathbf{M}_1$ as the coupling between the translational velocities of the floc and the force on the floc ($\mathbf{f}_t$), $\mathbf{M}_2$ as the coupling between the rotational velocities of the floc and the force on the floc, $\mathbf{M}_3$ as the coupling between the translational velocities of the floc and the torque on the floc ($\mathbf{0}$ in our scenario), and $\mathbf{M}_4$ as the coupling between the rotational velocities of the floc and the torque on the floc (Brady and Bossis, 1988). From Eqs. (16) and (17) the floc's linear and angular velocities can be calculated as

$$\mathbf{u} = \mathbf{M}_1 \mathbf{f}_t \tag{22}$$

$$\boldsymbol{\omega} = \mathbf{M}_2 \mathbf{f}_t \tag{23}$$

Because M_1 is a non-diagonal matrix, the linear velocity $\mathbf{u}$ is in general not parallel to the direction of gravity. If gravity acts in the z direction, the floc will have a vertical settling velocity $\mathbf{u}_z$ parallel to $\mathbf{f}_t$ and a horizontal drifting velocity $\mathbf{u}_{xy}$ perpendicular to $\mathbf{f}_t$. In addition to this translation, the floc will rotate about an axis, passing through the centre of action and not necessarily parallel to z, with angular velocity $\boldsymbol{\omega}$.

Being a symmetric, positive-definite matrix, $\mathbf{M}_1$ has three real and positive eigenvalues, and three corresponding eigenvectors. If the floc is oriented so that gravity acts along one of the eigenvectors, then the floc will maintain a velocity parallel to that eigenvector without lateral drift. The eigenvalues of $\mathbf{M}_1$ can be interpreted as scalar mobility coefficients, each of the 3 mobility coefficients representing the ratio of velocity and external force for translation along the corresponding eigenvector direction. The average hydrodynamic radius R_H of the floc is defined as (Lattuada et al., 2003)

$$R_H = \frac{1}{2\pi\mu\left(\alpha_1 + \alpha_2 + \alpha_3\right)}, \tag{24}$$

where α_1, α_2 and α_3 are the three eigenvalues of $\mathbf{M}_1$. Similarly, from the 3 eigenvalues β_1, β_2, β_3 of $\mathbf{M}_4$, the rotational hydrodynamic radius of the floc can be calculated as

$$R_\omega = \frac{1}{\left[\frac{8\pi\mu}{3}\left(\beta_1 + \beta_2 + \beta_3\right)\right]^{\frac{1}{3}}}. \tag{25}$$

While R_H and R_ω give a practically accurate quantification of the translation and rotation of the floc, their calculation requires knowledge of the corresponding mobility matrices. In contrast, the radius of the enclosing sphere R_{en} is straightforward to calculate from an experimental image of the floc. Therefore, finding a relation between R_{en} and the hydrodynamic radii is practically important.

In Fig. 5, R_H/R_{en} and R_ω/R_{en} are plotted versus R_{en}/a. For this plot, we have changed a from $R_{en}/5$ to $R_{en}/45$ keeping R_{en} fixed.

From the plot we can draw the following conclusions. First of all, R_H and R_ω are comparable in magnitude to R_{en}, but are both smaller than R_{en}. For all aggregates we observe that R_ω is slightly larger than R_H, although the difference is not large. Both R_H/R_{en} and R_ω/R_{en} decrease with increasing R_{en}/a for relatively large values of a, and reach a plateau for $R_{en}/a > 10$ approximately. This suggests that when the floc is represented by a group of fairly large spheres the resulting aggregates tend to *overestimate* the hydrodynamic resistance of the floc.

The radius of gyration is often used to characterise the geometric properties of flocs. Hence, to characterise the hydrodynamic behaviour of a floc the ratio R_H/R_G of hydraulic radius to radius of gyration has been quantified in several publications (Wiltzius, 1987; Van Saarloos, 1987; Gmachowski, 1996). These publications report a correlation between R_H/R_G and the fractal dimension. However limited, our data seem to confirm this trend. In Fig. 6a we have plotted R_H/R_G versus the number N of spheres of the aggregates used to represent the flocs S4, S5 and S6. The ratio R_H/R_G remains approximately constant for all three flocs as N increases, indicating that R_H/R_G can be quite independent of the number of beads composing the Stokesian Dynamics aggregate. We can see that S4 and S6, which have a similar fractal dimension, have also similar values of R_H/R_G. The floc S5, which has a smaller fractal dimension, has also a smaller value of R_H/R_G.

The voxel images of the three flocs (Fig. 1) show that the flocs are far from spherical. Actually it would be difficult to associate them to any regular geometry, even as an approximation. Floc S5 for example looks roughly like a short bent ribbon, while floc S6 is composed of a relatively compact structure with a linear branch coming out of it. On the other hand, the fractal dimension of the flocs is in between that of a sphere ($D_f = 3$) and of a disk ($D_f = 2$), so it is useful to compare the hydrodynamic radius of the flocs to these two regular shapes. The ratio R_H/R_G for a spherical aggregate, a disk-like aggregate, and a linear aggregate (chain) is plotted vs. N in Fig. 6(b). These regular aggregates are generated by assembling spherical beads, using a number of spheres N ranging from $O(10)$ to $O(1000)$, and the hydrodynamic radius calculated with the Stokesian Dynamics code. The accuracy of the calculation has been probed by comparing the solution for a chain to the analytical solution for a chain of spheres predicted by the slender body theory (Filippov, 2000). The excellent agreement between the values calculated from the slender body theory

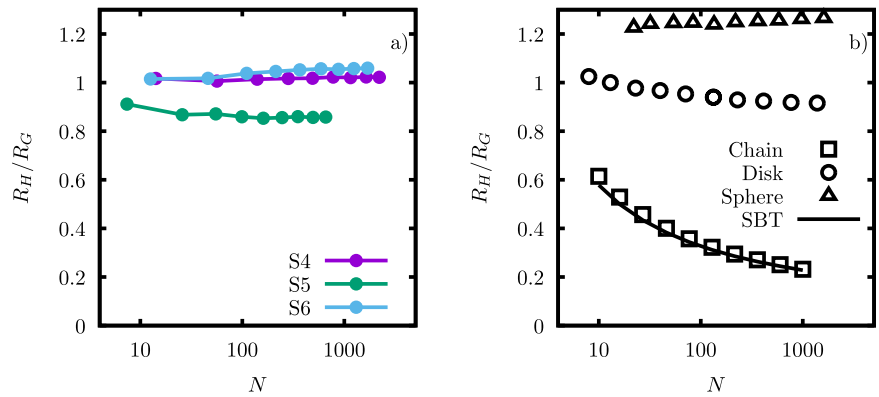

Fig. 6. The ratio R_H/R_G of the aggregates representing the floc S4, S5 and S6 are plotted as a function of the number N of primary spheres in (a). The value of N is increased by decreasing the primary sphere radius a, approximately following the scaling relationship shown in Fig. 4. As a comparison, the relation between R_H/R_G and N for a sphere, a disk and a chain of spheres is calculated in Stokesian dynamics and the result is shown in (b). The sphere, the disk and the chain represent the shape having the fractal dimension of 3.0, 2.0 and 1.0 respectively. The line (SBT) is the analytical solution $\frac{R_H}{R_G} = \frac{\sqrt{3}}{\ln(2N)}$.

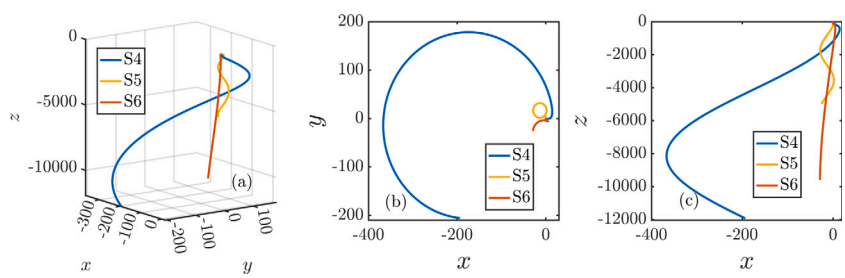

Fig. 7. Trajectories of the centroids of the three flocs during settling from $t = 0$ to $t = 500$. (a) 3-d view, (b) in the $x - y$ horizontal plane, and (c) in the $x - z$ vertical plane. Gravity is in the negative z direction.

and from the Stokesian dynamics for a 1D chain structure, and the ratio R_H/R_G for a spherical aggregate converging approximately to the theoretical value of $\sqrt{5/3} \approx 1.291$ expected for a smooth sphere, both provide the validation of our numerical methodology and actual code implementation.

From Fig. 6(a) and 6(b) we can see that for floc S4, S5 and S6 the slope of R_H/R_G versus N is nearly zero, smaller than the slope for sphere, which is slightly positive, and larger than the slope for disk, which is slightly negative. The results are consistent with the fact that the fractal dimensions of the three flocs considered in the current paper are bounded by the fractal dimensions of a sphere and disk. However, the value of R_H/R_G for S5 is significantly lower than the disk while its fractal dimension is larger than the disk. This apparent contradiction reveals that fractal dimension alone cannot fully capture hydrodynamic behaviour. While S5's mass distribution is more compact than a disk (higher fractal dimension), its internal porosity create smaller flow resistance, resulting in a smaller hydrodynamic radius relative to gyration radius. This highlights that hydrodynamic interactions depend not only on mass distribution but also on local permeability inaccessible to structural fractal analysis

4.3. Dynamic settling behaviour

After having considered in the previous section the hydrodynamic properties of each floc, we here look at the dynamics of sedimentation. Three aggregates are generated from the voxel images of flocs S4, S5 and S6 using spheres of radius $a = R_{en}/20$, containing 286, 98 and 217 spheres, respectively. The time step is chosen as 0.1 to ensure that each floc moves a distance of about $\approx 0.1R_{en}$ at each time step. The characteristic time is chosen as $a/u_{St,c}$ where $u_{St,c} = 2(\rho_s - \rho_f)a^2g/9\mu$.

We track the centroid of each floc over time (the centre of action of each floc coincides with the centroid because the density is the same for all the constituent particles). The trajectories of the three flocs starting from the position (0,0,0) are shown in Fig. 7. It is seen that the trajectories of flocs S4 and S5 are helical with a larger radius of curvature than that of floc S6. The axis of the helical motion is inclined, i.e. the flocs perform an average lateral drift while settling in a spiral motion (Fig. 7(b)). For floc S4, the maximum horizontal drift distance from its initial position is around 300, which is around $15R_{en}$. The trajectory of floc S4 for a longer time period is shown in Fig. 10(a), which shows more clearly a helical motion. For flocs S5, the maximum horizontal drift is around 40, which is $2R_{en}$. Floc S4 settles the fastest and floc S5 the slowest (Fig. 7(c)). Fig. 5(a) shows that to obtain a converged representation of the M_1 matrix, one needs at least 20 beads per unit R_{en}. Because the helical motion is primarily due to the properties of the M_1 matrix, we can estimate that helical motion we observe should not change provided that the geometry is discretised with at least 20 beads per unit R_{en}.

Time series of translational and rotational velocities are shown in Figs. 8 and 9, respectively. The translational velocities of S4 and S5 show a sinusoidal variation, which corresponds to the helical translational motion discussed above. The vertical velocity relaxes to a steady state value on a time scale much smaller than the time scale of this helical motion. The horizontal velocities of floc S4 for a longer time period are shown in Fig. 10(b), which show clear sinusoidal variations and a $\frac{1}{4}$-period phase lag between the velocities in the x and y directions, corresponding to the circular motion of floc S4 in the horizontal plane. Looking at the components of the rotational velocity, we notice that the axis of spinning motion around the centre of the floc is, predominantly, the direction of gravity. The finite rotational velocity components ω_x and ω_y at early times are transient and due to the reorientation of the floc from the initial configuration.

We can use Eq. (6) to estimate the floc settling velocities by setting $\theta = 6\pi$, $k = 1$, $l = aN^{1/3}$ (i.e., a sphere radius corresponding to a sphere

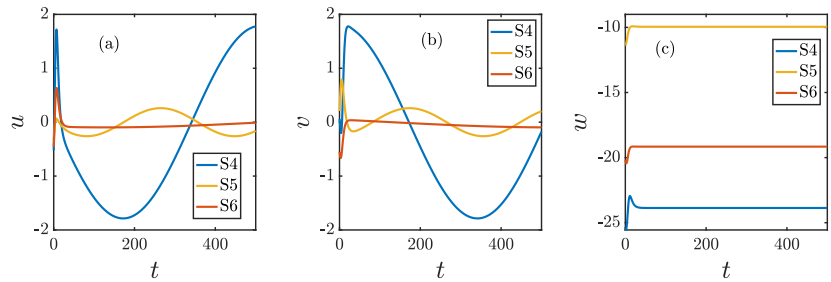

Fig. 8. Translational velocities of the flocs in (a) x, (b) y and (c) z directions.

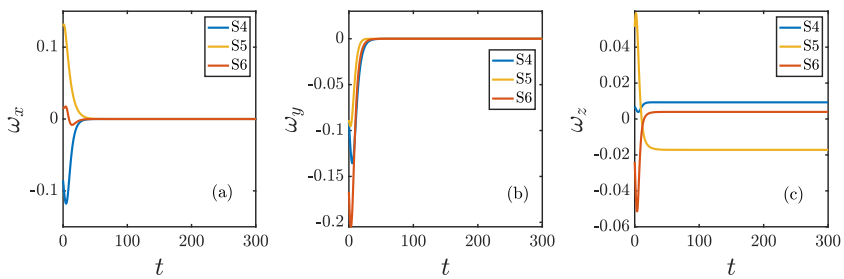

Fig. 9. Rotational velocities of the flocs in (a) x, (b) y and (c) z directions.

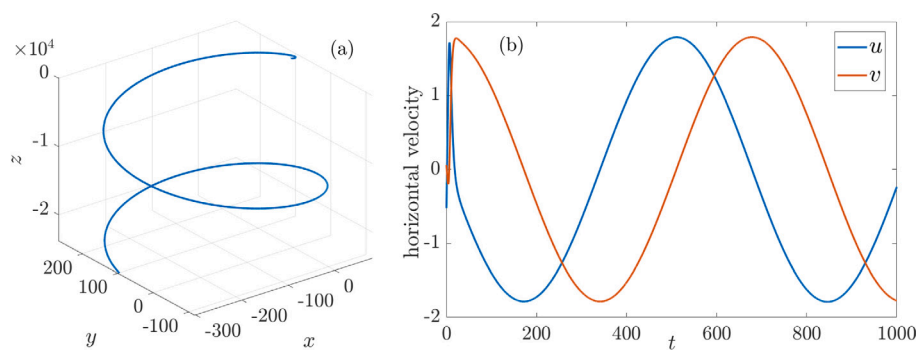

Fig. 10. (a) The trajectory and (b) horizontal translational velocities of floc S4 from $t = 0$ to $t = 1000$.

Table 2
Floc settling velocities rescaled by the Stokes velocity of the constituent spheres from simulations and estimations using Eq. (6).

Floc	Velocity from simulations	Velocity from estimations
S4	23.9	17.9
S5	10.0	7.4
S6	19.2	18.6

having the same volume of the floc) and D_f taken from Fig. 4. This rough estimate and the value computed from the dynamic simulations are compared in Table 2. The estimate tends to underestimate the settling velocities with a relative differences of about 25% for S4 and S5. Since all three flocs have the same R_{en}/a, the porosity decreases as the number of constituent spheres N increases, as shown in Eq. (20). Thus S4 is the least porous floc and S5 is the most porous floc. Thus, in our simulations the magnitude of the settling velocity increase as the porosity decreases.

In Figs. 11–13, we show instantaneous snapshots, at different times during settling. The observed configurations correspond well to the features seen in the time traces of translational and rotational velocity. For example, comparing the first two snapshots ($t = 0$ and $t = 100$), we see that each floc flips upside down, which corresponds to the rotation around the horizontal x and y axes for $t < 50$ seen in Fig. 9(a) and (b). After flipping upside down, each floc rotates about the vertical z axis (last four snapshots for each floc). Floc S5 rotates the fastest and floc S6 the slowest, as already discussed when introducing Fig. 9(c). These reconfigurations, which could conceivably be measured by optical experiments, produce immediate changes in the settling velocity because the flow has no inertia. A finite Reynolds number of the floc would produce a time lag between the hydrodynamic force and the instantaneous configuration.

5. Discussion and conclusion

Three-dimensional geometries of 3 natural sediment flocs sampled from the Thames Estuary, UK have been digitalised and converted into a realistic fluid dynamics model based on Stokesian Dynamics calculations, allowing us to calculate with high accuracy the viscous resistance to sedimentation and therefore the settling velocity. Output of the simulations is the full hydrodynamic resistance and mobility matrices, whose features are analysed in detail to get insight into the coupling between the gravitational force and translational/rotational motion. The radius of gyration of the 3 flocs have been calculated and compared with the computed hydrodynamic radius. The rotational dynamics of the floc, and its motion in the lateral direction (i.e. perpendicular to gravity) is also quantified. This work complements and extends previous analyses which were limited to synthetically-generated fractal flocs.

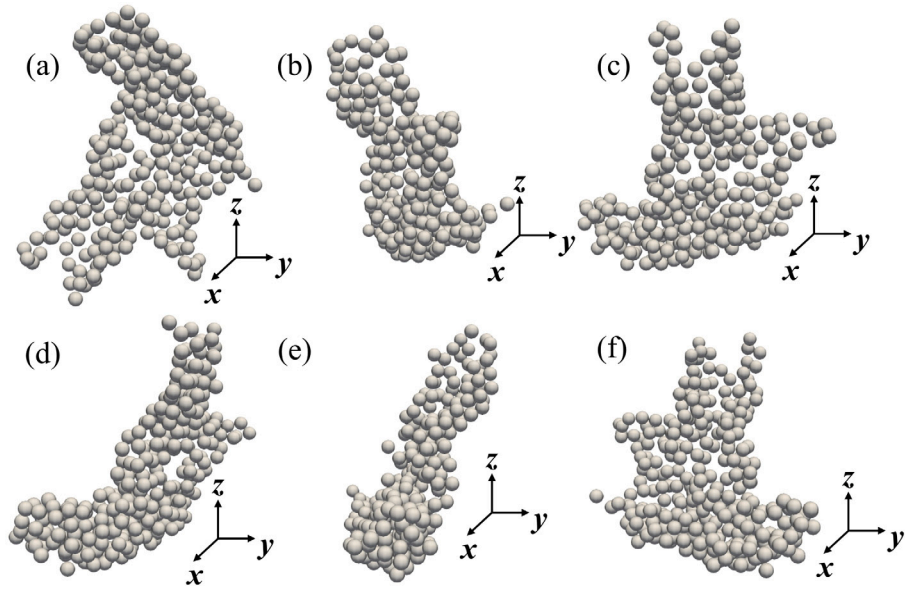

Fig. 11. Snapshots of floc S4 observed in the y–z plane with z in the vertical direction as it settles. From (a) to (f) t increases from 0 to 500 linearly.

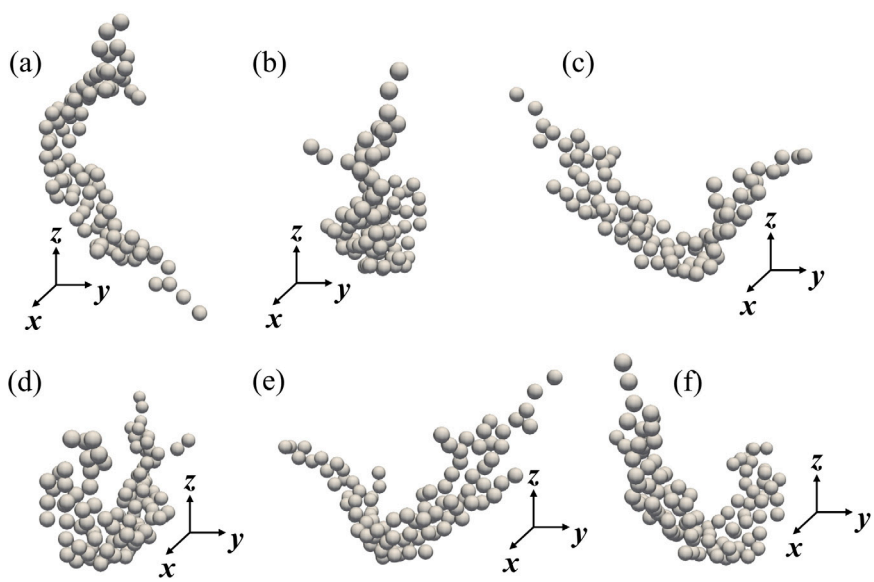

Fig. 12. Snapshots of floc S5 observed in the y–z plane with z in the vertical direction as it settles. From (a) to (f) t increases from 0 to 500 linearly.

Two of the flocs have a hydrodynamic radius, R_H, practically identical to the radius of gyration R_G. For the third floc, the ratio R_H/R_G is slightly smaller than the other two flocs despite a similar gross floc shape, but deviations of the ratio from 1 are relatively minor and therefore practically not very important. This result seem to support the widely-held assumption that accurate measurements of the radius of gyration from scanned experimental images – a purely geometry quantity – could give a good estimation of settling rates and sedimentation fluxes.

Spatial resolution of scanned images can be important. We found that capturing the hydrodynamic radius accurately requires representing the floc with beads of radius at least 1/30 smaller than the radius of smallest sphere completely circumscribing the floc; using larger beads, which corresponds to adopting a lower spatial resolution, leads to an overestimation of the actual hydrodynamic radius. In terms of experimental measurements, this result implies that coarse resolution of scanned images will tend to underestimate the true settling rate.

For a fractal-like flocs, the hydrodynamic resistance of the floc can be a function of the fractal dimension if the floc is highly fractal with $D_f < 2$. This dependence on fluid dynamics is often ignored in previous studies (Spencer et al., 2021; Smoczyński et al., 2016; Xu and Dong, 2017; Chapalain et al., 2019), which often assume that the main effect of the fractal geometry is to change only the effective density of the floc, rather than both the effective density and the hydrodynamic resistance to translational motion. For example, the formula for the settling rate of the classic book by Winterwerp and Van Kesteren (2004) is obtained by using the fractal dimension for the estimation of the effective weight of the floc (weight minus buoyancy) (see Eq. 4.6 in the book), but the formula for the drag force does not account for D_f (Eq. 5.1 in the book). The effect of fractal dimension on floc permeability has been appreciated in the past, see e.g. Binder et al. (2009) and references therein, but not calculated for realistic floc geometries. The consideration of a floc geometry that is not synthetic is the main contribution of the current paper.

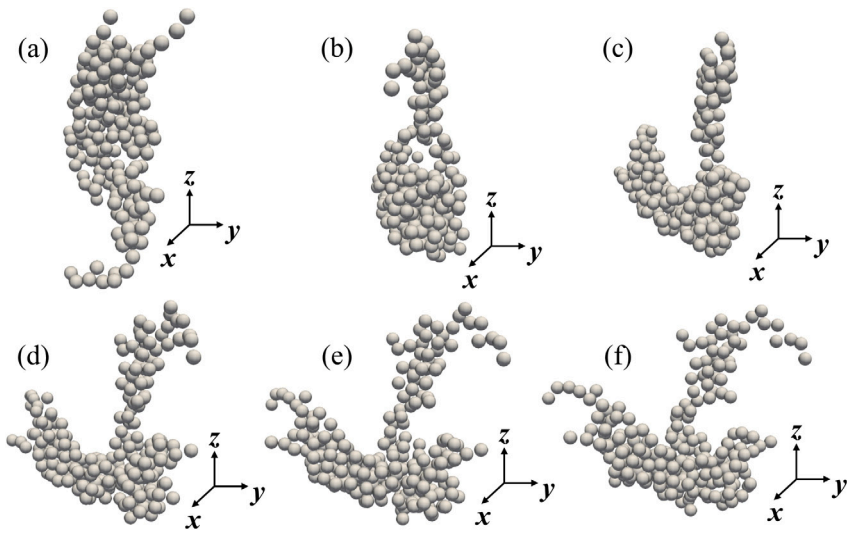

Fig. 13. Snapshots of floc S6 observed in the y–z plane with z in the vertical direction as it settles. From (a) to (f) t increases from 0 to 500 linearly.

The simulations reveal that the flocs can rotate while settling, performing an helical motion. This rotational motion is caused by the hydrodynamic interaction between different parts of the floc, which produce a coupling between the downward pointing gravitational force, the lateral floc velocity and its angular velocity. Because the lateral motion will effectively enlarge the collision radius of a floc, this observed lateral displacement could influence sediment transport fluxes by altering the rate of coagulation by differential sedimentation (Li and Botto, 2024). To illustrate the potential importance of this effect, we consider the following model for the rate of coagulation by differential sedimentation (Van Leussen, 1988):

$$\beta = \pi(r_i + r_j)^2 |w_i - w_j| \tag{26}$$

Here r_i and r_j are the average radii of the two flocs, and w_i and w_j are the corresponding settling velocities. While simple, this model, which is based on the advective flux of particles that cross a collisional area $\pi(r_i + r_j)^2$ surrounding a test particle i, is often used in practice because it capture the essential physics of flocs moving in rectilinear motion parallel to each other (Zhang and Zhang, 2011). If the flocs move in the lateral direction, performing a helical motion of radius $r_{helical,i} = \lambda r_i$, the collision area will increase by a factor dependent on λ. The model above predicts that the collision rate is enhanced by a factor λ^2, which can be significant for typical parameters. For example, using the results of Fig. 3 to estimate λ, we get $\lambda \approx 3$, which corresponds to an enhancement of the collision rate by almost an order of magnitude (our simulations suggest that the exact value of λ is dependent on the exact shape of the floc). While there are many parameters that could influence this enhanced collision rate (for example, the ratio of the pitch of the helix to the floc size), it is clear that because the floc size is small even small deviations from a straight sedimentation trajectory induced by floc shape anisotropy can play an important role in setting aggregation rates and deposition fluxes. Our observation of spiralling motion also links to the notion of "chirality" and its effect on sedimentation, recently explored in the fluid dynamics community using geometrically well-defined particles (Vaquero-Stainer et al., 2024; Melikhov and Ekiel-Jeżewska, 2025).

More broadly, our analysis represents a first step towards the development of a protocol to translate high-resolution experimental measurements of three-dimensional floc geometry to high-accuracy fluid dynamical calculation enabling to extract testable sedimentation parameters.

CRediT authorship contribution statement

Chuan Gu: Writing – review & editing, Writing – original draft, Visualization, Validation, Software, Methodology, Investigation, Formal analysis, Data curation. **Heng Li:** Writing – review & editing, Writing – original draft, Visualization, Validation, Software, Methodology, Investigation, Formal analysis, Data curation. **Kate L. Spencer:** Writing – review & editing, Writing – original draft, Supervision, Resources, Project administration, Funding acquisition, Conceptualization. **Lorenzo Botto:** Writing – review & editing, Writing – original draft, Supervision, Resources, Project administration, Methodology, Investigation, Funding acquisition, Formal analysis, Conceptualization.

Declaration of competing interest

The authors declare that they have no known competing financial interests or personal relationships that could have appeared to influence the work reported in this paper.

Acknowledgements

This research was supported by the UK Natural Environment Research Council (grant number NE/011678/1) and the European Research Council (ERC) under the European Union's Horizon 2020 research and innovation program (Grant Agreement No. 715475, project FLEXNANOFLOW).

Data availability

Data will be made available on request.

References

Agrawal, Y., Pottsmith, H., 1994. Laser diffraction particle sizing in STRESS. Cont. Shelf Res. 14 (10–11), 1101–1121.

Aidun, C.K., Lu, Y., Ding, E.-J., 1998. Direct analysis of particulate suspensions with inertia using the discrete Boltzmann equation. J. Fluid Mech. 373, 287–311.

Ali, W., Kirichek, A., Chassagne, C., 2024. Collective effects on the settling of clay flocs. Appl. Clay Sci. 254, 107399.

Baugh, J.V., Manning, A.J., 2007. An assessment of a new settling velocity parameterisation for cohesive sediment transport modeling. Cont. Shelf Res. 27 (13), 1835–1855.

Bernal, J.M.G., De La Torre, J.G., 1980. Transport properties and hydrodynamic centers of rigid macromolecules with arbitrary shapes. Biopolym.: Orig. Res. Biomol. 19 (4), 751–766.

Binder, C., Feichtinger, C., Schmid, H.-J., Thürey, N., Peukert, W., Rüde, U., 2006. Simulation of the hydrodynamic drag of aggregated particles. J. Colloid Interface Sci. 301 (1), 155–167.

Binder, C., Hartig, M.A., Peukert, W., 2009. Structural dependent drag force and orientation prediction for small fractal aggregates. J. Colloid Interface Sci. 331 (1), 243–250.

Bloomfield, V., Dalton, W., Van Holde, K., 1967a. Frictional coefficients of multisubunit structures. I. Theory. Biopolym.: Orig. Res. Biomol. 5 (2), 135–148.

Bloomfield, V., Van Holde, K., Dalton, W., 1967b. Frictional coefficients of multisubunit structures. II. Application to proteins and viruses. Biopolym.: Orig. Res. Biomol. 5 (2), 149–159.

Brady, J.F., Bossis, G., 1988. Stokesian dynamics. Annu. Rev. Fluid Mech. 20 (1), 111–157.

Carrasco, B., de la Torre, J.G., 1999. Hydrodynamic properties of rigid particles: comparison of different modeling and computational procedures. Biophys. J. 76 (6), 3044–3057.

Chapalain, M., Verney, R., Fettweis, M., Jacquet, M., Le Berre, D., Le Hir, P., 2019. Investigating suspended particulate matter in coastal waters using the fractal theory. Ocean. Dyn. 69, 59–81.

Derksen, J.J., 2014. Simulations of hindered settling of flocculating spherical particles. Int. J. Multiph. Flow 58, 127–138.

Dorrell, R., Hogg, A.J., 2010. Sedimentation of bidisperse suspensions. Int. J. Multiph. Flow 36 (6), 481–490.

Droppo, I.G., 2001. Rethinking what constitutes suspended sediment. Hydrol. Process. 15 (9), 1551–1564.

Droppo, I., Walling, D., Ongley, E., et al., 1998. Suspended sediment structure: implications for sediment and contaminant transport modelling. IAHS Publication, pp. 437–444.

Droppo, I., Walling, D., Ongley, E., et al., 2000. Influence of floc size, density and porosity on sediment and contaminant transport. (263), pp. 141–147, IAHS Publication(International Association of Hydrological Sciences).

Durlofsky, L., Brady, J.F., Bossis, G., 1987. Dynamic simulation of hydrodynamically interacting particles. J. Fluid Mech. 180, 21–49.

Dyer, K., Manning, A., 1999. Observation of the size, settling velocity and effective density of flocs, and their fractal dimensions. J. Sea Res. 41 (1–2), 87–95.

Filippov, A., 2000. Drag and torque on clusters of N arbitrary spheres at low Reynolds number. J. Colloid Interface Sci. 229 (1), 184–195.

Filippov, A., Zurita, M., Rosner, D., 2000. Fractal-like aggregates: relation between morphology and physical properties. J. Colloid Interface Sci. 229 (1), 261–273.

Gibbs, R.J., 1985. Estuarine flocs: their size, settling velocity and density. J. Geophys. Res.: Ocean. 90 (C2), 3249–3251.

Gmachowski, L., 1996. Hydrodynamics of aggregated media. J. Colloid Interface Sci. 178 (1), 80–86.

Guazzelli, E., Morris, J.F., 2011. A Physical Introduction to Suspension Dynamics, vol. 45, Cambridge University Press.

Happel, J., Brenner, H., 2012. Low Reynolds Number Hydrodynamics: with Special Applications to Particulate Media, vol. 1, Springer Science & Business Media.

Harshe, Y.M., Ehrl, L., Lattuada, M., 2010. Hydrodynamic properties of rigid fractal aggregates of arbitrary morphology. J. Colloid Interface Sci. 352 (1), 87–98.

Harshe, Y.M., Lattuada, M., 2012. Breakage rate of colloidal aggregates in shear flow through Stokesian dynamics. Langmuir 28 (1), 283–292.

Johnson, C.P., Li, X., Logan, B.E., 1996. Settling velocities of fractal aggregates. Environ. Sci. Technol. 30 (6), 1911–1918.

Khelifa, A., Hill, P.S., 2006. Models for effective density and settling velocity of flocs. J. Hydraul. Res. 44 (3), 390–401.

Kim, A.S., Stolzenbach, K.D., 2002. The permeability of synthetic fractal aggregates with realistic three-dimensional structure. J. Colloid Interface Sci. 253 (2), 315–328.

Kim, A.S., Yuan, R., 2005. Hydrodynamics of an ideal aggregate with quadratically increasing permeability. J. Colloid Interface Sci. 285 (2), 627–633.

Kirkwood, J.G., Riseman, J., 1948. The intrinsic viscosities and diffusion constants of flexible macromolecules in solution. J. Chem. Phys. 16 (6), 565–573.

Koch, D.L., Hill, R.J., 2001. Inertial effects in suspension and porous-media flows. Annu. Rev. Fluid Mech. 33 (1), 619–647.

Kranenburg, C., 1994. The fractal structure of cohesive sediment aggregates. Estuar. Coast. Shelf Sci. 39 (6), 451–460.

Kumar, R.G., Strom, K.B., Keyvani, A., 2010. Floc properties and settling velocity of san Jacinto estuary mud under variable shear and salinity conditions. Cont. Shelf Res. 30 (20), 2067–2081.

Lattuada, M., Wu, H., Morbidelli, M., 2003. Hydrodynamic radius of fractal clusters. J. Colloid Interface Sci. 268 (1), 96–105.

Lattuada, M., Wu, H., Morbidelli, M., 2004. Radial density distribution of fractal clusters. Chem. Eng. Sci. 59 (21), 4401–4413.

Lawrence, T., Carr, S., Wheatland, J., Manning, A., Spencer, K., 2022. Quantifying the 3D structure and function of porosity and pore space in natural sediment flocs. J. Soils Sediments 22 (12), 3176–3188.

Lesser, G.R., Roelvink, J.v., van Kester, J.T.M., Stelling, G., 2004. Development and validation of a three-dimensional morphological model. Coast. Eng. 51 (8–9), 883–915.

Li, H., Ali, W., Chassagne, C., Botto, L., 2025. Estimating the density of individual particles from the settling of a particle cloud. Front. Earth Sci. 13, 1710847.

Li, H., Botto, L., 2024. Hindered settling of a log-normally distributed Stokesian suspension. J. Fluid Mech. 1001, A30.

Liss, S.N., Droppo, I.G., Flannigan, D.T., Leppard, G.G., 1996. Floc architecture in wastewater and natural riverine systems. Environ. Sci. Technol. 30 (2), 680–686.

Maggi, F., Mietta, F., Winterwerp, J., 2007. Effect of variable fractal dimension on the floc size distribution of suspended cohesive sediment. J. Hydrol. 343 (1–2), 43–55.

Manning, A., Whitehouse, R., Uncles, R., 2017. ECSA practical handbooks on survey and analysis methods: Estuarine and coastal hydrography and sedimentology. pp. 211–260.

Maxey, M.R., Riley, J.J., 1983. Equation of motion for a small rigid sphere in a nonuniform flow. Phys. Fluids 26 (4), 883–889.

McCammon, J., Deutch, J., 1976. Frictional properties of nonspherical multisubunit structures. application to tubules and cylinders. Biopolym.: Orig. Res. Biomol. 15 (7), 1397–1408.

Mehta, A.J., 2013. An Introduction to Hydraulics of Fine Sediment Transport, vol. 38, World Scientific Publishing Company.

Melikhov, Y., Ekiel-Jeżewska, M.L., 2025. Dynamical modes of highly elastic loops settling under gravity in a viscous fluid. J. Fluid Mech. 1013, A13.

Rahmani, M., Gupta, A., Jofre, L., 2022. Aggregation of microplastic and biogenic particles in upper-ocean turbulence. Int. J. Multiph. Flow 157, 104253.

Rotne, J., Prager, S., 1969. Variational treatment of hydrodynamic interaction in polymers. J. Chem. Phys. 50 (11), 4831–4837.

Schwarz, C., Cox, T., Van Engeland, T., Van Oevelen, D., Van Belzen, J., Van de Koppel, J., Soetaert, K., Bouma, T.J., Meire, P., Temmerman, S., 2017. Field estimates of floc dynamics and settling velocities in a tidal creek with significant along-channel gradients in velocity and SPM. Estuar. Coast. Shelf Sci. 197, 221–235.

Smoczyński, L., Ratnaweera, H., Kosobucka, M., Smoczyński, M., Kalinowski, S., Kvaal, K., 2016. Modelling the structure of sludge aggregates. Environ. Technol. 37 (9), 1122–1132.

Sorensen, C.M., Roberts, G.C., 1997. The prefactor of fractal aggregates. J. Colloid Interface Sci. 186 (2), 447–452.

Spearman, J., Manning, A.J., 2008. On the significance of mud transport algorithms for the modelling of intertidal flats. In: Proceedings in Marine Science, vol. 9, Elsevier, pp. 411–430.

Spencer, K.L., Wheatland, J.A., Bushby, A.J., Carr, S.J., Droppo, I.G., Manning, A.J., 2021. A structure–function based approach to floc hierarchy and evidence for the non-fractal nature of natural sediment flocs. Sci. Rep. 11 (1), 14012.

Spencer, K., Wheatland, J., Carr, S., Manning, A., Bushby, A., Gu, C., Botto, L., Lawrence, T., 2022. Quantification of 3-dimensional structure and properties of flocculated natural suspended sediment. Water Res. 222, 118835.

Swan, J.W., Brady, J.F., Moore, R.S., 174, C., 2011. Modeling hydrodynamic self-propulsion with Stokesian dynamics. Or teaching Stokesian Dynamics to swim. Phys. Fluids 23 (7), 071901.

Swanson, E., Teller, D.C., de Haën, C., 1978. The low Reynolds number translational friction of ellipsoids, cylinders, dumbbells, and hollow spherical caps. Numerical testing of the validity of the modified oseen tensor in computing the friction of objects modeled as beads on a shell. J. Chem. Phys. 68 (11), 5097–5102.

Tambo, N., Watanabe, Y., 1979. Physical characteristics of flocs—I. The floc density function and aluminium floc. Water Res. 13 (5), 409–419.

Tozzi, E., Scott, C.T., Vahey, D., Klingenberg, D., 2011. Settling dynamics of asymmetric rigid fibers. Phys. Fluids 23 (3), 033301.

Vahedi, A., Gorczyca, B., 2012. Predicting the settling velocity of flocs formed in water treatment using multiple fractal dimensions. Water Res. 46 (13), 4188–4194.

Van Leussen, W., 1988. Aggregation of particles, settling velocity of mud flocs a review. In: Physical Processes in Estuaries. Springer, pp. 347–403.

Van Saarloos, W., 1987. On the hydrodynamic radius of fractal aggregates. Phys. A 147 (1–2), 280–296.

Vanni, M., 2000. Creeping flow over spherical permeable aggregates. Chem. Eng. Sci. 55 (3), 685–698.

Vaquero-Stainer, C., Miara, T., Juel, A., Pihler-Puzović, D., Heil, M., 2024. U-shaped disks in Stokes flow: chiral sedimentation of a non-chiral particle. J. Fluid Mech. 999, A71.

Veerapaneni, S., Wiesner, M.R., 1996. Hydrodynamics of fractal aggregates with radially varying permeability. J. Colloid Interface Sci. 177 (1), 45–57.

Villaret, C., Hervouet, J.-M., Kopmann, R., Merkel, U., Davies, A.G., 2013. Morphodynamic modeling using the Telemac finite-element system. Comput. Geosci. 53, 105–113.

Wheatland, J.A., Bushby, A.J., Spencer, K.L., 2017. Quantifying the structure and composition of flocculated suspended particulate matter using focused ion beam nanotomography. Environ. Sci. Technol. 51 (16), 8917–8925.

Wheatland, J.A., Spencer, K.L., Droppo, I.G., Carr, S.J., Bushby, A.J., 2020. Development of novel 2D and 3D correlative microscopy to characterise the composition and multiscale structure of suspended sediment aggregates. Cont. Shelf Res. 200, 104112.

Wiltzius, P., 1987. Hydrodynamic behavior of fractal aggregates. Phys. Rev. Lett. 58 (7), 710.

Winterwerp, J.C., 1998. A simple model for turbulence induced flocculation of cohesive sediment. J. Hydraul. Res. 36 (3), 309–326.

Winterwerp, J.C., Van Kesteren, W.G., 2004. Introduction to the Physics of Cohesive Sediment Dynamics in the Marine Environment. Elsevier.

Xu, C., Dong, P., 2017. A dynamic model for coastal mud flocs with distributed fractal dimension. J. Coast. Res. 33 (1), 218–225.
Yamakawa, H., 1970. Transport properties of polymer chains in dilute solution: hydrodynamic interaction. J. Chem. Phys. 53 (1), 436–443.
Yu, Z., Niu, X., 2024. The motion of three-dimensional fractal aggregates in homogeneous shear flow. Phys. Fluids 36 (1).
Zhang, Z., Botto, L., Prosperetti, A., 2006. Microstructural effects in a fully-resolved simulation of 1,024 sedimenting spheres. In: IUTAM Symposium on Computational Approaches To Multiphase Flow. Springer, pp. 197–206.
Zhang, J.-F., Zhang, Q.-H., 2011. Lattice Boltzmann simulation of the flocculation process of cohesive sediment due to differential settling. Cont. Shelf Res. 31 (10), S94–S105.
Zhu, Z., Hu, R., Lei, Y., Shen, L., Zheng, X., 2022. Particle resolved simulation of sediment transport by a hybrid parallel approach. Int. J. Multiph. Flow 152, 104072.